Geochemistry, Geophysics, Geosystems®

AGU ADVANCING EARTH AND SPACE SCIENCE

RESEARCH ARTICLE
10.1029/2021GC010160

Key Points:

- The interaction between volcanic jets with glacial meltwater can further fragment pyroclasts fining the grain size distribution
- By integrating a volcanic jet model with grain size measurements we estimate the water-to-melt ratio in the 10th century Eldgjá eruption
- The interaction of a volcanic jet with glacial meltwater can lead to eruption plume collapse, depending on water-to-melt mass ratio

Supporting Information:

Supporting Information may be found in the online version of this article.

Correspondence to:

S. Hajimirza,
sahand@rice.edu

Citation:

Hajimirza, S., Jones, T. J., Moreland, W. M., Gonnermann, H. M., & Thordarson, T. (2022). Quantifying the water-to-melt mass ratio and its impact on eruption plumes during explosive hydromagmatic eruptions. *Geochemistry, Geophysics, Geosystems*, *23*, e2021GC010160. https://doi.org/10.1029/2021GC010160

Received 14 SEP 2021
Accepted 20 JAN 2022

Author Contributions:

Conceptualization: Thomas J. Jones, Helge M. Gonnermann, Thor Thordarson
Data curation: William M. Moreland
Methodology: Sahand Hajimirza, Thomas J. Jones, William M. Moreland, Helge M. Gonnermann
Visualization: Sahand Hajimirza, Thomas J. Jones
Writing – original draft: Sahand Hajimirza, Thomas J. Jones
Writing – review & editing: Sahand Hajimirza, Thomas J. Jones, William M. Moreland, Helge M. Gonnermann, Thor Thordarson

Quantifying the Water-to-Melt Mass Ratio and Its Impact on Eruption Plumes During Explosive Hydromagmatic Eruptions

Sahand Hajimirza[1], Thomas J. Jones[2], William M. Moreland[3], Helge M. Gonnermann[1], and Thor Thordarson[3]

[1]Department of Earth, Environmental, and Planetary Sciences, Rice University, Houston, TX, USA, [2]Department of Earth, Ocean and Ecological Sciences, University of Liverpool, Liverpool, UK, [3]Faculty of Earth Sciences, University of Iceland, Reykjavík, Iceland

Abstract The interaction of magma with external water commonly enhances magma fragmentation through the conversion of thermal to mechanical energy and results in an increased production of fine-grained volcanic tephra. Magma-water interaction is thus of importance for hazard mitigation on both a local and a regional scales. The relative proportion of water that interacts with magma, quantified as the water-to-melt mass ratio, is thought to determine the efficiency of thermal to mechanical energy conversion, termed the fragmentation efficiency. Here, we analyze the pyroclast size distributions from the 10th century Eldgjá fissure eruption in Iceland, where parts of the fissure erupted subglacially and other erupted subaerially. The subglacially erupted magma passed through a column of glacial meltwater, resulting in a larger proportion of finer pyroclast sizes relative to the subaerially erupted, purely magmatic tephra. This finer grain size distribution has been attributed to quench-granulation induced by enhanced cooling upon interaction with external water. We hypothesize that the additional fragmentation (surface) energy required to produce the finer grained hydromagmatic deposits is due to the conversion of thermal to mechanical energy associated with the entrainment of water into the volcanic jet, as it passed through a column of subglacial melt water. Based on field and granulometry data, we estimate that the interaction of the volcanic jet with the meltwater provided an additional fragmentation energy of approximately 3–14 kJ per kg of pyroclasts. We numerically model the hydrofragmentation energy within a jet that passes through a layer of meltwater. We find that the water-to-melt mass ratio of entrained water required to produce the additional fragmentation energy is in the range of 1–2, which requires a minimum ice melting rate of 10^4 m^3 s^{-1}. Our simulation results show that the water-to-melt ratio is an important parameter that controls the ascent of plume in the atmosphere.

1. Introduction

Phreatomagmatism or hydromagmatism is common on this water-bearing planet, Earth, because the magma is often erupted through water bodies such as lakes, ice-melts in cauldrons and the shallow seas (Houghton et al., 2015). In such events the magma is typically fully vesiculated and disintegrated by gas expansion at the point of coming into contact with the external water (e.g., Carey et al., 2009; Liu et al., 2015, 2017; Moreland et al., 2019). For example, in Iceland, within glacier-derived tephra is associated with 75% of the events in the Holocene stratigraphy (Thordarson & Hoskuldsson, 2008), therefore, understanding vesicular magma-water interaction is of great relevance. In cases where the ice is relatively thick (>500 m), eruptions are typically effusive and build subglacial edifices (Edwards et al., 2015). Furthermore, the resulting landforms have been used as paleoclimate proxys to constrain the extent and thickness of ice sheets (e.g., Edwards et al., 2011; Russell et al., 2013; Smellie et al., 2008; Wilson et al., 2018). Eruptions beneath relatively thin ice (<200 m), melt the ice to form a steep-sided caldron, often filled with meltwater (Edwards et al., 2015). This was the case for some of the eruptive vents from the 10th century Eldgjá fissure eruption in Iceland (Figure 1), and is the focus here.

Interaction of volcanic jets with external water, that is water other than that originally dissolved within the erupting magma, can impact the jet dynamics. The entrained ambient water into the jet may condense and cause the jet to collapse or the water may vaporize and increase the jet buoyancy and thus the stability of the eruption (Cahalan & Dufek, 2021; Head & Wilson, 2003; Koyaguchi & Woods, 1996; Rowell et al., 2021; Van Eaton et al., 2012). Moreover, interaction of volcanic jets with external water can further fragment primary magmatic pyroclasts, by secondary hydrofragmentation processes. For all other conditions remaining the same, hydrofragmentation is more energy consuming than the pure magmatic fragmentation in "dry" eruptions (e.g., Wohletz et al., 2013

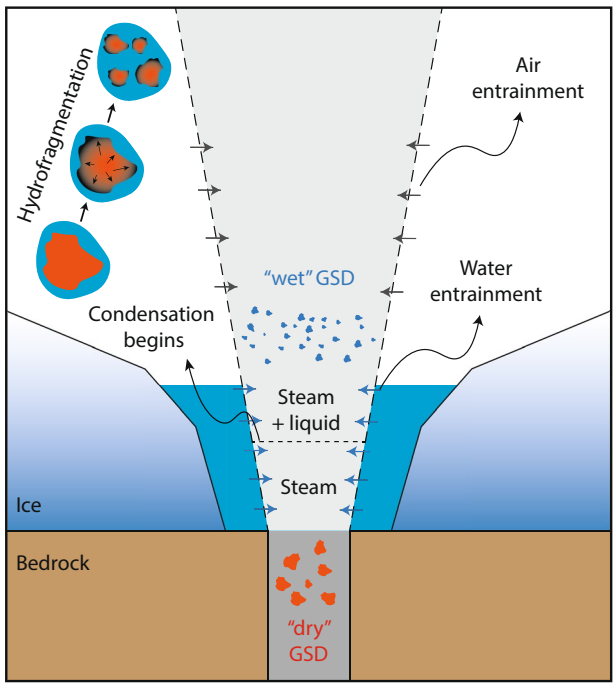

Figure 1. A schematic of a subglacial explosive eruption with a pyroclastic jet erupting within an ice cauldron. The "dry," already fragmented, magma undergoes further (secondary) hydrofragmentation as external glacial meltwater is entrained into the volcanic jet. Due to the interaction of external water with the magma, the fragmentation process includes thermal granulation due to rapid quenching of the magma and fragmentation due to vapor film boiling. Here, dry GSD refers to grain size distribution prior to the interaction of the volcanic jet with external meltwater, whereas wet GSD is the grain size distribution after the interaction.

and references therein). Consequently, hydromagmatic eruptions tend to have enhanced fine ash production relative to dry eruptions (Carey et al., 2009; Fitch & Fagents, 2020; Fitch et al., 2017; Graettinger et al., 2013; Houghton & Hackett, 1984; Liu et al., 2015, 2017; Mastin et al., 2004).

Hydrofragmentation is thought to occur by two main processes: thermal granulation during direct contact between melt and water, and vapor film formation and collapse (Wohletz et al., 2013). Thermal granulation occurs when the thermal stresses induced by rapid cooling overcome the tensile strength of the quenching melt (Colombier et al., 2019; Kokelaar, 1986; Van Otterloo et al., 2015). The fragmentation processes associated with vapor film formation are more complex. When the water at the melt-water interface becomes heated above the Leidenfrost temperature, repeated cycles of vapor film formation, expansion, and collapse occur. During this process, instabilities form and fragment the magma at the magma-water interface (Colombier et al., 2018; Eckhoff, 2016; Iskhakov et al., 2019; Koshizuka et al., 1999; Meignen et al., 2014; Sheridan & Wohletz, 1983; Sonder et al., 2018; Van Otterloo et al., 2015).

There is growing evidence that during many hydromagmatic eruptions the magma has already fragmented by primary magmatic processes before it interacts with external water (Aravena et al., 2018; Carey et al., 2009; Houghton & Carey, 2019; Liu et al., 2017; Moreland et al., 2019). From detailed textural studies of the Eldgjá deposits (Moreland et al., 2019), we know that the vesicular magma was already fragmented by magmatic processes prior to the interaction with external water. Deposits erupted from both subaerial and subglacial vents have near identical bubble number densities and bubble size distributions (Moreland et al., 2019). This suggests that both parts of the eruptive fissure had a similar magma ascent rates (Toramaru, 1990) and thus, similar magma discharge rates and conduit geometries (Wilson et al., 1980). Moreover, the primary magmatic fragmentation energy is thought to be mainly dependent on the balance between decompression rate and the rate of gas escape from magma, which itself is controlled by vesicle texture (Rust & Cashman, 2011). Therefore, identical bubble size distributions observed in the Eldgjá deposits implies that both the subaerial and subglacial parts of the eruption had similar magmatic fragmentation energies and produced similar grain size distributions prior to interaction with the external meltwater. Thus, the difference in specific surface energy between the hydromagmatic and purely magmatic deposits, provides direct evidence of the hydrofragmentation energy involved (Figure 1).

The extent of hydrofragmentation is controlled by the conversion of thermal to mechanical energy (Wohletz, 1986; Wohletz et al., 2013). The efficiency of this energy conversion depends on a large number of factors, including the confining geometry, the ambient pressure, the physical properties of the melt, and the water-to-melt ratio (Aravena et al., 2018; Board et al., 1974; Kokelaar, 1986; Pedrazzi et al., 2013; Sheridan & Wohletz, 1981; Wohletz & Sheridan, 1983). The latter will be the focus of this study, specifically the relationship between the extent of magma-water interaction, quantified as the melt-to-water ratio, and the extent of hydrofragmentation, quantified in terms of specific surface area of the pyroclastic deposit. Although the relationship between water-to-melt ratio and fragmentation energy has been experimentally investigated, it is extremely difficult to quantify for volcanic eruptions (Büttner & Zimanowski, 1998; Büttner et al., 2002, 2006; Colombier et al., 2019; Mastin, Spieler, & Downey, 2009; Schmid et al., 2010; Sheridan & Wohletz, 1983; Wohletz, 2002; Wohletz & McQueen, 1984; Zimanowski et al., 1997). Here, we use the estimates of hydrofragmentation energy for 10th century Eldgjá eruption in conjunction with a numerical model to constrain the water-to-melt mass ratio present in the volcanic jet during the subglacial eruption. Moreover, we examine the impact of this ratio on the ascent of the eruption plume in the atmosphere. The water-to-melt mass ratio directly controls how much of the water condenses in the jet, which itself determines whether the jet becomes a stable buoyant plume or collapses (Koyaguchi & Woods, 1996; Rowell et al., 2021).

2. The 10th Century Eldgjá Eruption

Eldgjá is an approximately 70 km long fissure system (Larsen, 2000; Miller, 1989) associated with the Katla central volcano in the south of Iceland (Figure 2). The fissure is classified as a mixed cone row type and is arranged into discrete segments in an en echelon arrangement. It stretches between the Mýrdalsjökull and Vatnajökull glaciers, and the south-westernmost 12 km of the fissure is located beneath the Mýrdalsjökull glacier

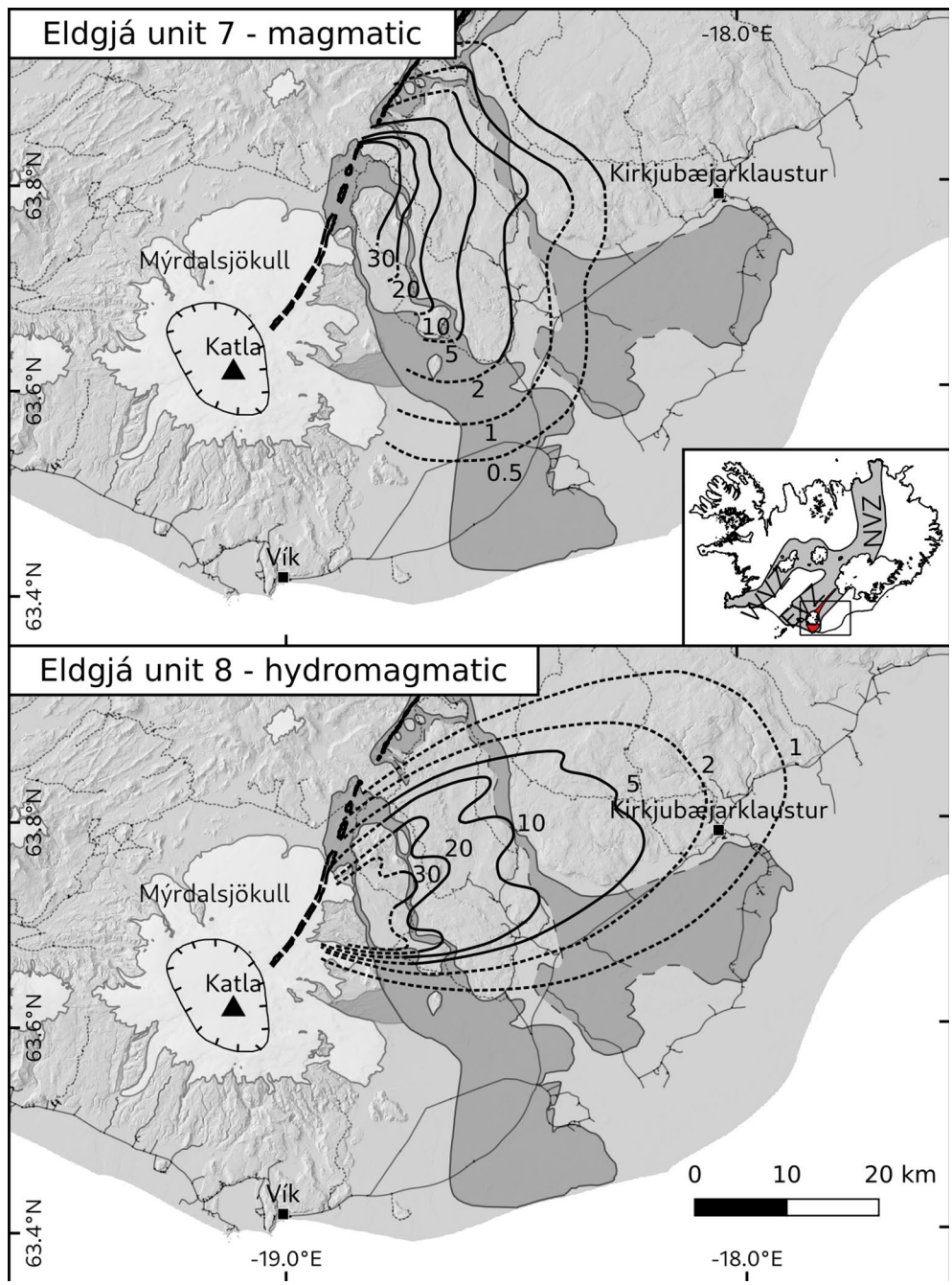

Figure 2. Overview of the 10th century Eldgjá eruption magmatic (top panel) and hydromagmatic (bottom panel) deposits, after Moreland et al. (2019). Inset shows the location of the field area in the Eastern Volcanic Zone of Iceland. The eruptive fissure segments are marked by thick black lines. Dark and light gray shading represents Eldgjá lava flow deposits and glaciers respectively. The fine black lines are isopachs, with thickness values shown in cm. Isopachs are dashed in areas where inadequate data was available for reconstruction.

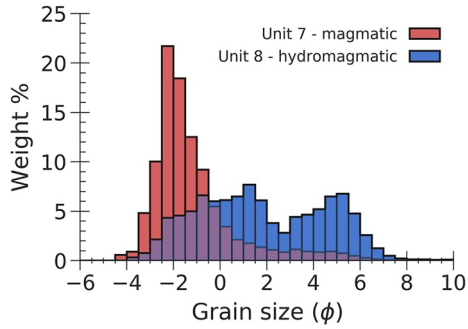

Figure 3. Total grain size distributions for the magmatic subaerial Unit 7 (red) and the hydromagmatic subglacial Unit 8 (blue) episodes of the 10th century Eldgjá eruption, Iceland, after Moreland et al. (2019). The grain size of the pyroclasts is expressed in terms of ϕ, where $\phi = -\log_2 (d\ (\text{mm}))$ and d is the grain diameter.

(Thordarson & Larsen, 2007; Thordarson et al., 2001). Based on ice-cores, environmental records, and medieval sources, the start of the eruption has been variously dated to 934 CE (Hammer, 1984; Stothers, 1998), 938 CE (Zielinski et al., 1995), and 939 CE (McCarthy & Breen, 1997; Oman et al., 2006; Oppenheimer et al., 2018). The eruption was dominantly effusive producing 19.7 km^3 of lava (Sigurdardóttir et al., 2015), but included at least 16 explosive episodes (Moreland et al., 2019) over a total eruptive time of at least 1.5 years (Oppenheimer et al., 2018) and potentially as long as 3–8 years (Thordarson et al., 2001; Zielinski et al., 1995).

Tephra from the eruption comprises at least 16 distinct pyroclasts fallout units produced by periodic explosive phases dispersed throughout the eruption and separated by considerable time intervals (Moreland et al., 2019). During the explosive episodes a significant volume of tephra (approximately 1.3 km^3 dense rock equivalent) was produced (Larsen, 2000). Explosive activity began with subglacial episodes in the south-west and subsequent episodes generally took place at even more north-easterly locations along the fissure. However, there were at least four occasions when explosive activity shifted to within-glacier locations (Moreland et al., 2019). The Eldgjá tephra deposit is exceptionally thick with over 4 m of tephra accumulated at 10 km from the vent. Because there were both subaerial and within-glacier fissure segments the Eldgjá tephra deposit represents a composite of magmatic and hydromagmatic tephra.

We focus our study on two distinct eruption units: Unit 7, which is solely composed of magmatic tephra and Unit 8, which is hydromagmatic (Moreland et al., 2019). Unit 7 originated from the subaerial southern Eldgjá fissure segment (Figure 2) and formed a poly-lobate deposit (Moreland et al., 2019). The tephra of Unit 7 is black to metallic blue in color, is very well to well sorted (Moreland, 2017) in the proximal to medial regions (<20 km from source). Unit 8 has a brown color and is lacking in achneliths, consistent with a cooler and wetter eruption environment. Based on the tephra distribution, Unit 8 originated from a short length of the subglacial fissure beneath Mýrdalsjökull. It is well to poorly sorted (graphic standard deviation of 1.62–3.59 ϕ [Moreland, 2017]) in the proximal to medial regions.

Although deposits can be identified along the entire vent system, individual tephra units can be directly linked to specific vent regions along the fissure. Here, we model the eruption of Unit 7 and 8 deposits as emanating from localized vents that localized along the Eldgjá fissure system. This assumption is based on abundant observations that basaltic fissure eruptions often lead to prolonged eruptive activity from localized vents (Bruce & Huppert, 1989; Eibl et al., 2017; Jones & Llewellin, 2021; Jones et al., 2017; Neal et al., 2019; Parcheta et al., 2015). Especially for subglacial eruptions, the formation of localized ice cauldrons and vents seems to be the rule, rather than the exception (Edwards et al., 2015). This assumption is also consistent with the Unit 7 and 8 isopachs (Figure 2). Nevertheless, it is a simplifying assumption upon and our results are limited to eruption from localized vents, as opposed to the less likely scenario that the Unit 7 and 8 deposits were erupted over a prolonged period from a high aspect ratio, fissure-like vent.

Total deposit grain-size distributions of each unit were calculated by Moreland (2017) and exhibit a significant difference between magmatic and hydromagmatic deposits (Figure 3). The grain size distribution of the magmatic Unit 7 is positively skewed and unimodal with a median grain-size diameter of −2.2 ϕ. The distribution of the hydromagmatic Unit 8 is bimodal with peaks at 0.0 ϕ and 5.0 ϕ. Despite the strong difference between the total grain-size distributions, Moreland et al. (2019) demonstrated that the vesicle-size distribution for Eldgjá magmatic and hydromagmatic tephra are identical. This indicates that, regardless of whether the vent was subaerial or subglacial, the ascending magma underwent similar bubble nucleation and growth processes up to the point of fragmentation and quenching.

The volume of each unit was calculated by Moreland (2017) using the exponential method (Pyle, 1995), resulting in 0.024 km^3 dense rock equivalent for Unit 7 and 0.029 km^3 dense rock equivalent for Unit 8. The column height for the episodes producing Units 7 and 8 was estimated to be between 11 and 17 km, and 17 and 18 km, respectively (Moreland, 2017). Using the empirical relationship between height and eruption rate of Mastin, Guffanti,

Table 1
List of Parameters and Associated Symbols

A	Surface area of tephra
b	Plume radius
C_a	Specific heat of air at constant pressure
C_{pc}	Specific heat of pyroclasts at constant pressure
E	Specific energy flux
ΔE_s	Specific surface energy
$\hat{E}_f$	Specific hydrofragmentation energy
g	Gravity
h	Specific enthalpy
H_1	Height of tropopause
H_2	Height of stratosphere
h_{amb}	Specific enthalpy of ambient fluid
M	Momentum flux
n_{ps}	Mass ratio of pyroclasts
n_w	Mass ratio of water in plume
n_w^{amb}	Mass ratio of water in ambient fluid
n_a	Mass ratio of air
n_a^{amb}	Mass ratio of air in ambient fluid
P_w^{amb}	Pressure in ambient meltwater
P_a^{amb}	Atmospheric pressure
P_0	Reference atmospheric pressure
Q	Mass discharge rate
T	Temperature
T_a^{amb}	Atmospheric temperature
T_r	Reference temperature
u	Mixture velocity
u_{amb}	Inward velocity of entrained fluid
$\dot{W}_{frag}$	The rate of hydrofragmentation energy
z	Distance above the vent
Z_w	Depth of glacial meltwater
ρ	Mixture density
ρ_w	Density of water
ρ_a	Density of air
ρ_{pc}	Density of pyroclasts
ρ_{amb}	Ambient fluid density
ϵ	Entrainment coefficient
γ	Surface energy density
β	Conversion factor of thermal to hydrofragmentation energy
μ	Temperature gradient in troposphere
ω	Temperature gradient in stratosphere

et al. (2009); Mastin, Spieler, & Downey (2009), corresponding mass eruption rates are between 9×10^6 and 2×10^7 kg s^{-1}, and 1×10^7 to 3×10^7 kg s^{-1} for Units 7 and 8, respectively.

3. Methods

3.1. Fragmentation Energies From Grain Size Distributions

Figure 3 shows the total grain size distributions (TGSD) obtained by Moreland et al. (2019). The TGSD that resulted from dry magmatic fragmentation is shown in red and subglacial hydromagmatic fragmentation is shown in blue. The difference in these two TGSDs can be accounted for by a difference in the extent of fragmentation (surface area). The additional fragmentation energy, ΔE_s (J kg^{-1}), required to transform a unit mass of magmatic tephra into the hydromagmatic tephra is given by

$$\Delta E_s = \gamma \, \Delta A, \tag{1}$$

where ΔA (m^2 kg^{-1}), is the difference in surface area per unit mass of tephra and, γ (J m^{-2}), is the fracture surface energy density of basaltic glass (Dürig et al., 2012). This parameter is slightly different to the specific surface energy used in related work (Buhl et al., 2014; Büttner & Zimanowski, 1998; Chester et al., 2005; Grady, 1982; Griffith, 1921; Yew & Taylor, 1994) because γ in Equation 1 accounts for all energies that affect the fracture process (e.g., heat and ductile deformation), which we consider to be most representative of the natural process. Furthermore, γ has been well characterized for silicate glass (Dürig et al., 2012). The list of all the parameters used in this study, and their associated symbols, is provided in Table 1.

To calculate the surface area per unit mass for both TGSDs shown in Figure 3, we treated all particles as spherical with a median diameter corresponding to the measured grain size bins. Using the bulk tephra densities measured by Moreland (2017), we estimated the number of clasts within each grain size bin. The surface area of all the particles was then summed to give the total surface area per unit mass. We consider that the difference in surface area between the magmatic and hydromagmatic deposits, denoted as ΔA, represents the additional fragmentation due to water-magma interaction. Here we calculated ΔA using particle sizes in aggregate. This is justified because hydrofragmentation at Eldgjá is thought to be by quenched granulation (Moreland et al., 2019) of already fragmented pyroclasts that underwent a secondary fragmentation. Consequently, the distinction of "active particles" that are relevant in primary hydrofragmentations of fuel-coolant type (Fitch et al., 2017) is not applicable here. Using a range of fracture surface energy densities between 40 and 130 J m^{-2} (Dürig et al., 2012), we then estimated a range of additional specific fragmentation energies associated with hydromagmatic fragmentation of Unit 8 using Equation 1.

3.2. Conceptual Model for Estimating the Water-to-Melt Mass Ratio

To estimate the water-to-melt mass ratio we simulated the dynamics of a volcanic jet rising above the vent and passing through a column of glacial meltwater and continuing upward in the atmosphere as a buoyant plume. At the vent the jet is a mixture of pyroclasts and exsolved magmatic volatiles. As the jet passes through the column of glacial meltwater, it entrains meltwater at freezing temperature. The entrained meltwater mixes within the jet and reduces the bulk jet temperature. The heat transferred from magma to the entrained meltwater is treated as instantaneous and the resultant mixture is considered to be at thermal

equilibrium at all times. As long as the mixture temperature remains above the water boiling temperature, the entrained meltwater vapourizes and expands in volume. The associated mechanical work due to this volumetric expansion is converted into both kinetic and hydrofragmentation energies. Other types of energy (e.g., seismic and acoustic) are neglected here. We calculate the hydrofragmentation energy expended during jet ascent within the meltwater column by assuming it is proportional to the thermal energy provided by the pyroclasts.

Above the meltwater surface, the jet rises in the atmosphere, and entrains and mixes with air which decreases the bulk jet density. Once the bulk density of the jet decreases below the density of the atmosphere, the jet becomes a buoyant plume and continues to rise in the atmosphere. The total amount of external water entrained into the jet governs the mixture density and temperature and, in turn, ultimately determines whether the pyroclastic mixture is able to rise upward as a buoyant plume, or becomes negatively buoyant and collapses. The total flow rate of entrained meltwater is calculated by integrating the flow rate of entrained water over the entire height of the meltwater column. The water-to-melt ratio is then calculated by dividing the total flow rate of entrained meltwater by the flow rate of pyroclasts. Lastly, we constrained our estimates of the water-to-melt ratio in two ways. First, by matching the predicted hydrofragmentation energy with the measured additional surface energy of pyroclasts. Second, by matching the predicted plume height with the interpreted values from pyroclasts dispersal.

3.3. Pyroclastic Jet and Plume Model

To simulate the volcanic jet passing through a column of meltwater and the subsequent plume rising buoyantly in the atmosphere we solved the one-dimensional steady conservation equations for a volcanic jet and plume (Mastin, 2007; Woods, 1988). Following these previous works, in this study we treat the jet as a homogeneous mixture of pyroclasts, water, and air, all in thermal equilibrium. Any fallout of the pyroclastic materials from the jet is neglected and all phases are assigned to be completely mixed at all times and thus treated as a homogeneous bulk mixture of a given velocity, u. Furthermore, the effect of vent geometry, mixture overpressure relative to the ambient fluid, turbulent flow development on entrainment rate are neglected (Mastin, 2007). Accepting these approximations, the conservation of mass, momentum, and energy for the mixture are given by (Mastin, 2007)

$$\frac{dQ}{dz} = \frac{d\left(\pi b^2 \rho u\right)}{dz} = 2\pi b \rho_{\text{amb}} u_{\text{amb}}, \tag{2}$$

$$\frac{dM}{dz} = \frac{d(Qu)}{dz} = \pi b^2 \left(\rho_{\text{amb}} - \rho\right) g, \tag{3}$$

and

$$\frac{dE}{dz} = \frac{d}{dz}\left(Q\left(\frac{u^2}{2} + gz + h\right)\right) = \left(gz + h_{\text{amb}}\right)\frac{dQ}{dz} - \frac{d\dot{W}_{\text{frag}}}{dz}, \tag{4}$$

respectively, where variables are defined in Table 1.

$\dot{W}$ is the rate of hydrofragmentation energy consumption which we assign as proportional to the thermal energy of pyroclasts, and to the ratio between the mass flow rate of entrained water and the mass flow rate of the jet. During air entrainment above the meltwater column, we assume the energy used for fragmentation is negligible. This is because expansion energy of entrained air is insignificant compared to meltwater being vapourized. Given these approximations, $\dot{W}$ is given by

$$\frac{d\dot{W}_{\text{frag}}}{dz} = \begin{cases} \beta\left(n_{\text{pc}} Q C_{\text{pc}}\left(T - T_{\text{r}}\right)\right)\dfrac{dQ/dz}{Q} & \text{for } z \le Z_{\text{w}} \\ 0 & \text{for } z > Z_{\text{w}} \end{cases} \tag{5}$$

where Z_w is the height of meltwater column and β is a conversion factor that determines the percentage of the pyroclasts' thermal energy that is converted into hydrofragmentation energy. In the case of adiabatic steam expansion during magma water interaction, β varies approximately between 2% and 15% depending on a number of factors such as the melt temperature and the water-to-melt mass ratio (Wohletz & McQueen, 1984; Wohletz

et al., 2013). Here, we approximate β as a constant throughout each simulation run and estimate the total calculated specific energy required to produce the particles from

$$\hat{E}_{\mathrm{f}} = \frac{1}{Q n_{\mathrm{pc}}} \int_0^{Z_{\mathrm{w}}} \frac{d\dot{W}_{\mathrm{frag}}}{dz}, \tag{6}$$

for each simulation run we find the value of Z_w by matching the specific hydrofragmentation energy with the additional surface energy measurement, $\hat{E}_{\mathrm{f}} = \Delta E_{\mathrm{s}}$.

The variations in the mass fractions of water, n_w, and air, n_a, in the mixture are given by (Mastin, 2007)

$$\frac{dn_{\mathrm{w}}}{dz} = \frac{dQ}{dz}\frac{1}{Q}\left(n_{\mathrm{w}}^{\mathrm{amb}} - n_{\mathrm{w}}\right) \tag{7}$$

and

$$\frac{dn_{\mathrm{a}}}{dz} = \frac{dQ}{dz}\frac{1}{Q}\left(n_{\mathrm{a}}^{\mathrm{amb}} - n_{\mathrm{a}}\right) \tag{8}$$

respectively. Here, $n_{\mathrm{w}}^{\mathrm{amb}}$ and $n_{\mathrm{a}}^{\mathrm{amb}}$ are the mass fraction of water and air in the ambient fluid, respectively. During the meltwater entrainment, $z \le Z_W$, $n_{\mathrm{a}}^{\mathrm{amb}} = 0$, and $n_{\mathrm{w}}^{\mathrm{amb}} = 1$. At $z > Z_W$, air is taken to be dry and hence $n_{\mathrm{a}}^{\mathrm{amb}} = 1$ and $n_{\mathrm{w}}^{\mathrm{amb}} = 0$. The mass fraction of pyroclasts is calculated from

$$n_{\mathrm{pc}} + n_{\mathrm{water}} + n_{\mathrm{air}} = 1. \tag{9}$$

the surrounding meltwater is considered to be at temperature of 0°C and the hydrostatic pressure decreases with height above the vent as

$$P_{\mathrm{w}}^{amb} = \rho_{\mathrm{w}}^{\mathrm{amb}} g\left(Z_{\mathrm{w}} - z\right). \tag{10}$$

to calculate the ambient temperature of air we use the formulation of Woods (1988) given by

$$T_{\mathrm{a}}^{amb} = \begin{cases} T_{\mathrm{r}} + \mu z & \text{for } z < H_1, \\ T_{\mathrm{r}} + \mu H_1 & \text{for } H_1 \le z \le H_2, \\ T_{\mathrm{r}} + \mu H_1 + \omega\left(z - H_2\right) & \text{for } z > H_2. \end{cases} \tag{11}$$

where $T_r = 273$ K is the reference temperature, $H_1 = 10$ km and $\mu = -6.5$ K km^{-1} are the height of tropopause and temperature gradient in the troposphere, respectively. $H_2 = 20$ km and $\omega = 2$ K km^{-1} are the height and temperature gradient in the stratosphere, respectively. Specifying that ambient air follows the ideal gas law, the hydrostatic pressure in the atmosphere is calculated as

$$\frac{dP_{\mathrm{a}}^{\mathrm{amb}}}{P_{\mathrm{a}}^{\mathrm{amb}}} = -\frac{g}{R_{\mathrm{a}} T_{\mathrm{a}}^{\mathrm{amb}}} dz, \tag{12}$$

where R_a is the gas constant for air. The resultant atmospheric pressure is

$$P_{\mathrm{a}}^{\mathrm{amb}} = \begin{cases} P_0\left(1 + \frac{\mu z}{T_{\mathrm{r}}}\right)^{\frac{-g}{R_a \mu}} & \text{for } z < H_1; \\ P_0\left(1 + \frac{\mu H_1}{T_{\mathrm{r}}}\right)^{\frac{-g}{R_a \mu}} \exp\left(-\frac{g\left(z - H_1\right)}{R_{\mathrm{a}}\left(T_{\mathrm{r}} + \mu H_1\right)}\right) & \text{for } H_1 \le z \le H_2; \\ P_0\left(1 + \frac{\mu H_1}{T_{\mathrm{r}}}\right)^{\frac{-g}{R_a \mu}} \exp\left(-\frac{g\left(H_2 - H_1\right)}{R_{\mathrm{a}}\left(T_{\mathrm{r}} + \mu H_1\right)}\right)\left(1 + \frac{\omega\left(z - H_2\right)}{T_{\mathrm{r}} + \mu H_1}\right)^{\frac{-g}{R_a \omega}} & \text{for } z > H_2 \end{cases} \tag{13}$$

where $P_0 = 1$ atm is the reference pressure. The mixture is set to be at thermal equilibrium at all values of z and temperature is calculated from the mixture enthalpy. After calculating enthalpy from Equation 4 temperature is estimated from

$$h = n_{\mathrm{pc}} C_{\mathrm{pc}} (T - T_{\mathrm{r}}) + n_{\mathrm{w}} h_{\mathrm{w}} + n_{\mathrm{a}} C_{\mathrm{a}} (T - T_{\mathrm{r}}), \tag{14}$$

where C_{pc} and C_a are the specific heats of pyroclasts and air at constant pressure, respectively. $T_r = 273$ K is a reference temperature, and the h_w is the specific enthalpy of water. Depending on the temperature and pressure, water may exist as vapor, liquid, ice or a mixtures thereof. Here, we ascribe water to be in its equilibrium state at all elevations. These water properties are calculated based on Wagner and Pruβ (2002) for liquid water and vapor and based on Feistel and Wagner (2006) for ice. The calculation of T requires an iteration at each integration step of the governing differential equations, whereby T is predicted from an initial guess and is iteratively corrected until Equation 14 is satisfied. After finding T, the mixture density is calculated from

$$\frac{1}{\rho} = \frac{n_{\mathrm{pc}}}{\rho_{\mathrm{pc}}} + \frac{n_{\mathrm{w}}}{\rho_{\mathrm{w}}} + \frac{n_{\mathrm{a}}}{\rho_{\mathrm{a}}}, \tag{15}$$

where ρ_{w} is the density of water, ρ_{pc} is the density of pyroclasts and assumed to be a constant. ρ_{a} is the density of air in the mixture and it is estimated from the ideal gas law.

A key variable in our simulations is the volume flux of meltwater or ambient air across the outer perimeter of the jet and plume. The volume flux is denoted as u_{amb} and also referred to as the entrainment rate. The entrainment of ambient fluid (i.e., water or air in this study) into the plume is facilitated by turbulent shear instabilities that form continuously between the upward flowing plume and the stationary ambient fluid with a relatively similar density to the plume. u_{amb} is typically considered to be proportional to the plume velocity. This has been shown to be a robust relation (Morton, 1959), with the proportionality constant, termed the entrainment coefficient, ϵ, here assumed constant with a value of 0.09 typically used for volcanic plumes (Mastin, 2007; Woods, 1988). Furthermore, Mastin, Guffanti, et al. (2009) and Mastin, Spieler, & Downey (2009) have demonstrated that this entrainment coefficient is appropriate by comparing model results with observed plume heights. Here, we use the formulation of Woods (1988) to account for the difference in density between the jet and the ambient fluid for the momentum-driven jet ascending within the meltwater column and the atmosphere (Mastin, 2007; Woods, 1988). In the momentum-driven jet the inward velocity of the ambient fluid is given by

$$u_{\mathrm{amb}} = \epsilon u \sqrt{\rho / \rho_{\mathrm{amb}}}, \tag{16}$$

and in the buoyancy driven plume it is given by

$$u_{\mathrm{amb}} = \epsilon u, \tag{17}$$

where the factor $\sqrt{\rho / \rho_{\mathrm{amb}}}$ accounts for density differences between the jet and the ambient fluid.

We solve the system of differential Equations 2–4 and 7 and 8 using a Runge-Kutta method. At the vent where z = 0 m, the jet is assumed to contain, 0.5 wt% of magmatic water (Budd et al., 2016) and 1000 ppm CO_2 at temperature of 1100°C (Hartley et al., 2014). Similar to air in the mixture, CO_2 is approximated as an ideal gas. We consider a mass discharge rate at the vent of 10^7 kg s^{-1}, which is interpreted from ash dispersal data (Moreland, 2017). Using this mass discharge rate we perform simulations for a range of initial velocities. For each simulation we use a conversion factor, β, that falls within a range of 2%–15%. We estimate Z_{w} such that the calculated specific fragmentation energy is equal to the additional specific surface energy of Unit 8, $\hat{E}_{\mathrm{f}} = \Delta E_{\mathrm{s}}$.

4. Results

4.1. Specific Surface Energy for Hydromagmatic and Magmatic Tephra Deposits

The tephra density was measured by Moreland (2017) who reports the magmatic and hydromagmatic tephra deposits to have bulk densities ranging from 560 to 1100 kg m^{-3} and from 590 to 720 kg m^{-3}, respectively. This density range was used to compute the range of possible surface areas listed in Table 2. Using these densities and the fracture surface energy densities measured for basaltic glass by Dürig et al. (2012), we estimate the difference in specific surface energy between magmatic to hydromagmatic tephra as 3.12–14.43 kJ kg^{-1} (Table 2).

Table 2
Calculation Results of Specific Surface Energy, E_s, Upon Varying Input Parameters (Hydromagmatic Deposit Surface Area, Surface Area Created, Fracture Surface Energy Density)

Variable	Values	Unit	Reference
Surface area of magmatic tephra	12–23	$m^2\ kg^{-1}$	(Moreland, 2017)
Surface area of hydromagmatic tephra	101–123	$m^2\ kg^{-1}$	(Moreland, 2017)
Surface area created (ΔA)	78–111	$m^2\ kg^{-1}$	This study
Fracture surface energy density (γ)	40–130	$J\ m^{-2}$	(Dürig et al., 2012)
Additional specific surface energy (ΔE_s)	3,120–14,430	$J\ kg^{-1}$	This study

4.2. Jet Modeling Results

Figure 4 shows a representative example of the simulation results for a case without external meltwater ($Z_w = 0$ m), a case with glacial meltwater thickness of $Z_w = 60$ m, and a case where $Z_w = 30$ m. The initial jet velocity for all the three cases is 150 m s^{-1} Figures 4a–4d represent the evolution of jet properties during meltwater entrainment, through the water column only. Jet velocity increases with distance above the vent (Figure 4a), as meltwater is entrained, heated, and evaporated, it decreases the mixture density (Figure 4b). Initially, at the proximal distances to the vent, when the mixture temperature is above the condensation temperature of water, sensible heat transfer from the jet to the entrained water causes the jet temperature to decrease rapidly (Figure 4c). As mixture temperature reaches the condensation temperature of water, the heat transfer from the jet to the entrained water becomes latent which, rather than reducing temperature, causes steam to condense at a relatively constant temperature. As the mass fraction of liquid water to vapor increases, the mixture density increases rapidly and the mixture velocity decreases. This is especially notable in the case where the meltwater layer thickness is 60 m. The hydrofragmentation (surface) energy is predicted to increase rapidly at first, when the temperature is above the boiling temperature, but slows down as the temperature reaches the boiling point (Figure 4d). Therefore, our simulations suggest that the majority of additional surface area is created during the first 10 m of jet ascent in the meltwater column where temperatures are higher and hence more thermal energy is available. The thickness of the meltwater layer in all cases is defined such that once the jet reaches the top of the meltwater layer, the specific hydrofragmentation energy reaches 14 kJ kg^{-1}, which is equivalent to the additional specific surface energy of the hydromagmatic tephra at Eldgjá.

Figures 4e–4h show our simulation results within and above the meltwater column. In the case with no meltwater the plume is predicted to reach 16 km elevation before the upward velocity reaches zero and the plume spreads laterally. In this case, with distance above the vent, the mixture velocity decreases rapidly because of the downward buoyancy force on the jet exiting the meltwater column (Figure 4e). Once the jet entrains enough air and becomes positively buoyant, its velocity slightly increases and remains relatively constant with height before the plume stops rising and spreads laterally. In the case where $Z_w = 30$ m, the plume reaches an elevation of more than 17 km, which is slightly higher than the elevation reached by the dry plume. In this case, the velocity initially increases from 150 to 250 m s^{-1} as the jet passes through the meltwater column. Once the jet enters into the atmosphere, its velocity decreases rapidly with height, but increases again once the plume becomes positively buoyant. The increase in velocity is, in this case, more substantial than in the dry plume because the entrained water increases the internal energy of the plume. This allows the plume to sustain a slightly higher temperature whilst entraining cold atmospheric air, and thus yields a higher buoyancy relative to the dry plume case. In the case where $Z_w = 60$ m, the plume collapses at a height below 1 km because the mass fraction of condensed water in the jet is too high to allow the jet to become buoyant.

5. Discussion

We simulated the jet dynamics for different values of β between 2% and 15%. For each β we solved for a meltwater column height, plume height and water-to-melt ratio such that the estimated hydrofragmentation energy matched the additional surface energy observed in the hydromagmatic tephra, ΔE_s (Figure 5). For high conversion factors, β > 10%, only a few centimeters of meltwater is required to match the measured surface energy, whereas for β = 2%, the required height of meltwater column is greater than 70 m. Among this wide range of

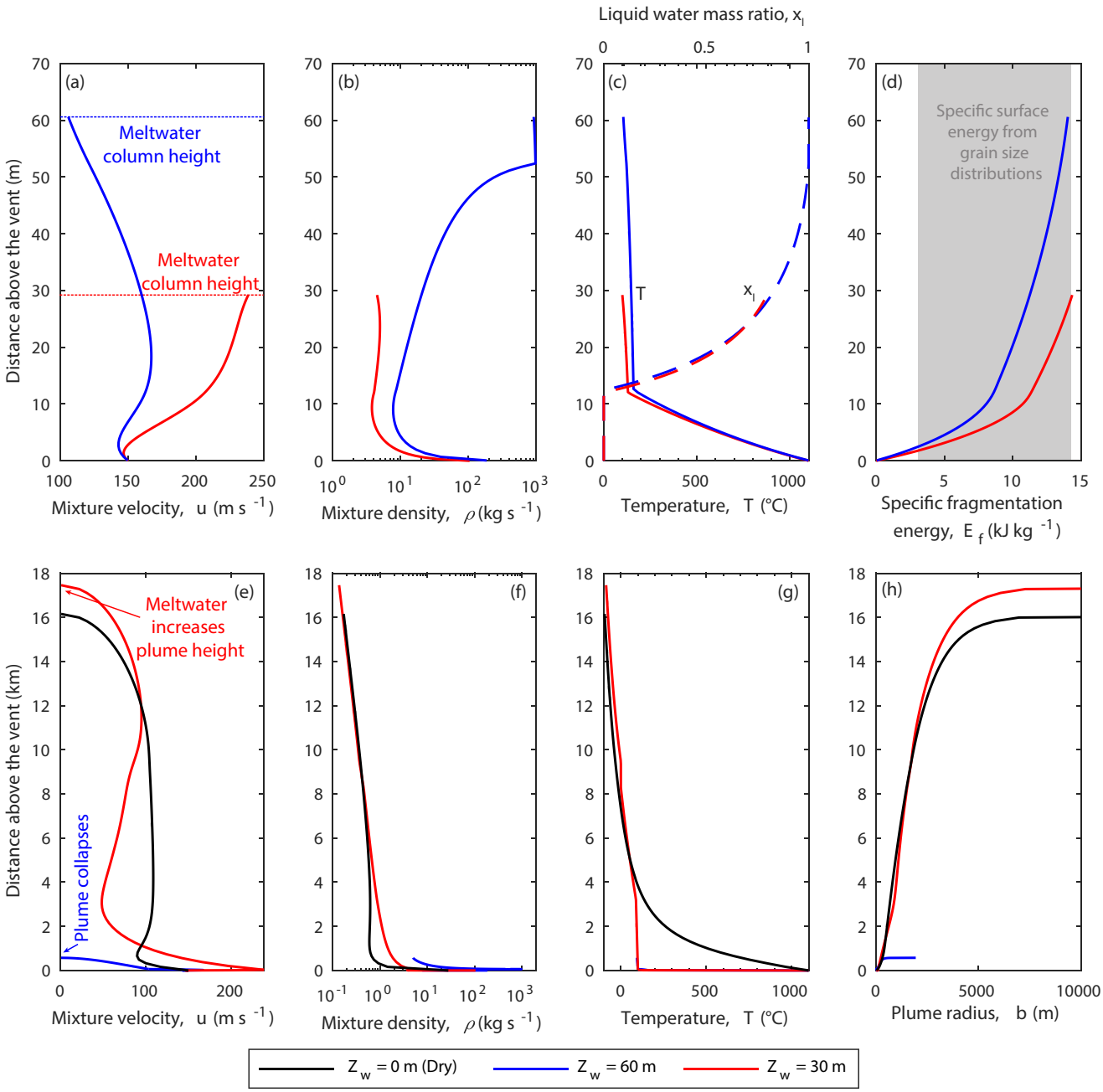

Figure 4. The evolution of jet properties with distance above the vent for three different meltwater heights, Z_W = 60, 30, and 0 m (i.e., no meltwater/dry). Figure panels in the top row show results for the jet rising in meltwater, whereas the second row panels show results for the jet rising in the meltwater and atmosphere. All cases have identical initial conditions at the vent, $Q = 10^7$ kg s^{-1}, T = 1100°C, n_w = 0.5 wt%, u = 150 m s^{-1}, except the initial pressure which is calculated uniquely, based on the height of the meltwater column.

estimated meltwater column heights, however, only model simulations with $Z_w < 35$ m produce plume heights that are comparable with the interpretations from fallout deposits. At meltwater depths of greater than 35 m our model predicts that the plume will collapse because the increase in density due to vapor condensation does not allow the jet to become buoyant (Koyaguchi & Woods, 1996; Rowell et al., 2021).

The plume height interpreted from ash dispersal data for the subaerial eruption phase (Unit 7) is 11–17 km, whereas it is slightly higher, 17–18 km, for the subglacial eruption phase (Unit 8; Moreland, 2017). This slight increase in plume height in the subglacial eruptions has previously been interpreted as an indicative of increase

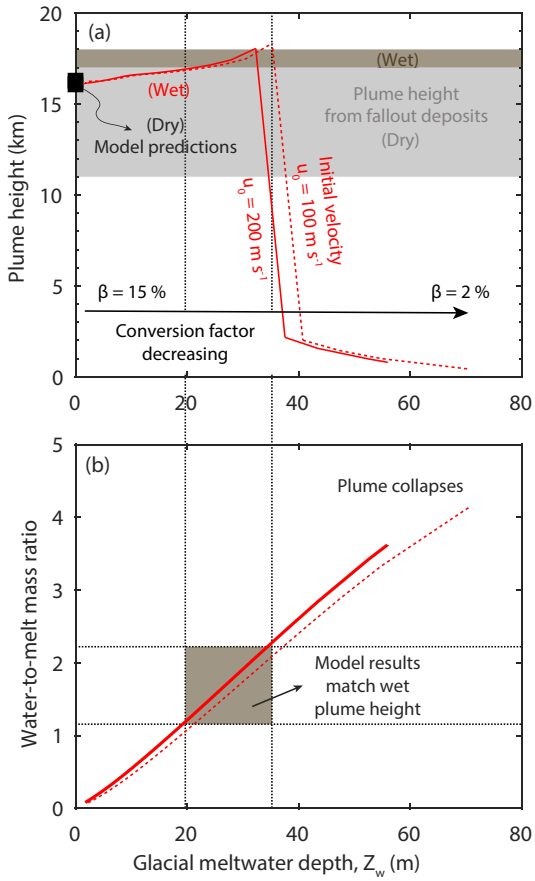

Figure 5. Estimated meltwater depth, plume height, and the water-to-melt mass ratio for different values of conversion factor $\beta = 2\%–15\%$ allowing the simulated specific fragmentation energy to match the measured values. The estimated water depth varies from less than 1–70 m. However, only those simulations with meltwater depth less than 35 m match the inferred plume heights, shown by the brown and gray shaded areas, for dry and wet phases of the eruption, respectively. Water-to-melt ratios in the range between 1 and 2 match the interpreted wet plume heights.

in the mass discharge rate at the subglacial vent (Moreland et al., 2019). However, our simulation results show that, with identical exit conditions at the vent, mixtures that pass through meltwater can reach higher elevations than dry plumes (Figure 4). This is true for situations where the thermal energy of the jet is high enough to vapourize all, or most of, the entrained meltwater (Koyaguchi & Woods, 1996; Rowell et al., 2021). Our findings therefore suggest that the relative increase in the plume height in the subglacial phase might be due the entrainment of glacial meltwater. Assuming this to be the case, and that the subaerial and subaerial parts of the eruption had identical mass discharge rates at the vent, the estimated depth of meltwater during the 10th Century Eldgjá fissure eruption is constrained between 20 and 35 m (Figure 5).

We determine the water-to-melt mass ratio for each simulation run by calculating the ratio of the total mass flow rate of meltwater entrained into the jet to the mass flow rate of pyroclasts. We find that simulated plumes will collapse if the water-to-melt ratio is greater than 2. For the case of Eldgjá, plume heights matching those interpreted from the fallout deposits are achieved when the water-to-melt mass ratio is between 1 and 2 (Figure 5b). Given a mass discharge rate of $\sim 10^7$ kg s^{-1} at the peak eruption intensity (Moreland, 2017), the associated meltwater entrainment rate is $(1–2) \times 10^7$ kg s^{-1}. The rate of ice melting required to sustain this rate of water entrainment would be at least $(1–2) \times 10^4$ m^3 s^{-1}. Note that this is a minimum value given the assumption that all of the meltwater becomes entrained into the jet. In comparison with other Icelandic subglacial eruptions our estimate of melting rate for Eldgjá is higher (Figure 6). The estimated rate of ice melting during the 2010 Eyjafjallajökull is ≈400–2000 m^3 s^{-1} at peak eruption intensity with a magma discharge rate of $(0.4–1) \times 10^6$ kg s^{-1} (Gudmundsson et al., 2012), which is an order of magnitude smaller than Elgdjá. During the 1996 Gjálp eruption the melting rate was 1,160–5,800 m^3 s^{-1} at the peak eruption intensity with a magma discharge rate of $(1–4) \times 10^6$ kg s^{-1} (Gudmundsson et al., 1997, 2004; Figure 6). This implies that ice melting rate is proportional to magma discharge rate.

We recognize that there are some simplifying assumptions in our simulations that require further investigation in future studies. We assumed that the entrained water will completely mix with the jet. However, the mixing is likely partial where the center of the jet remains mostly isolated from the entrained meltwater for some jet heights (Cahalan & Dufek, 2021; Head & Wilson, 2003). In this case, only the thermal energy of the mixed pyroclasts can be converted into fragmentation energy. Therefore, for a given conversion factor (β), a higher degree of water and jet interaction would be required to produce a given hydrofragmentation energy. This suggests that our estimates of meltwater column height and water-to-melt mass ratio are a lower bound. Moreover, we assumed that the jet has the same pressure as the ambient fluid at the vent. Consequently, water entrainment begins at the vent rather than after some length over which the jet decompresses to the ambient pressure. This assumption could lead to underestimation of the meltwater column height, but has little impact on the estimated melt-water mass ratio. We neglected the transfer of thermal energy into seismic, acoustic or other types of energy, which would reduce the estimated fragmentation energy by a relatively modest amount.

We assumed that the conversion ratio of thermal to hydrofragmentation energy remains constant over the entire ascent through the meltwater column. Studies of magma-water interaction suggest that the conversion ratio depends on a number of factors such as confining geometry, the ambient pressure, the physical properties of the melt, and water-to-melt mass ratio (Aravena et al., 2018; Board et al., 1974; Kokelaar, 1986; Pedrazzi et al., 2013; Sheridan & Wohletz, 1981; Wohletz & Sheridan, 1983). However, these studies that have constrained the conversion factor for magma and water interaction were for an instantaneous contact between stationary melt and water,

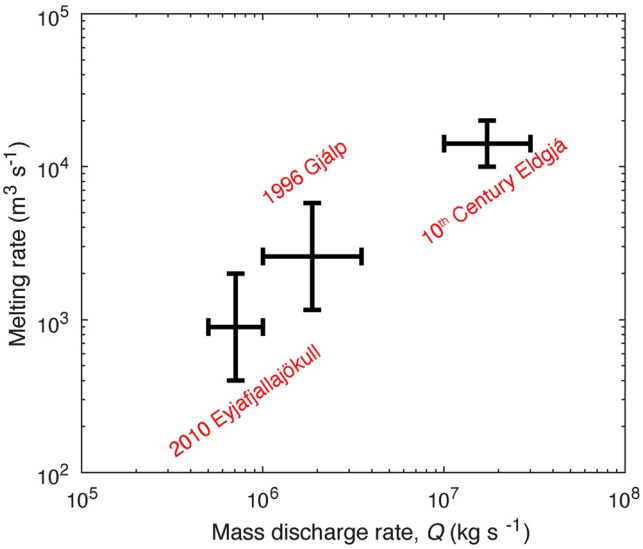

Figure 6. The ice melting rate for the subglacial phases of three eruptions in Iceland. The data for the 10th century Eldgjá eruption is from this study, for 2010 Eyjafjallajökull is from Gudmundsson et al. (2012), and for 1996 Gjálp is from Gudmundsson (2003) and Gudmundsson et al. (1997). The error bars represent the variation in mass discharge rate and ice melting rate over the climactic phase of the eruptions. Prior to the eruptions the ice thickness in Eyjafjallajökull was approximately 2 km and in Gjálp it was approximately 5 km.

whereas during meltwater and jet interaction, water is entrained and mixes within a dynamic jet. Further experimental and theoretical studies are therefore required to constrain the conversion of the pyroclasts thermal energy into fragmentation energy within dynamic volcanic jets. Our simulations therefore provide a key, first step in constraining water entrainment and any associated hydrofragmentation for explosive eruptions that pass through a water column (e.g., subglacial meltwater, and crater lakes).

6. Conclusions

For the first time we have been able to quantify the water-to-melt ratio for a subglacial eruption using total grain size distribution data. Our approach was used to interrogate the 10th century Eldgjá fissure eruption in Iceland, however our methods could be equally applied to other historic subglacial or subaqueous explosive eruptions. It is observed that hydromagmatic pyroclasts associated with eruption from subglacial vents have distinctively finer grain size distributions than purely magmatic tephra from subaerial eruptions. At Eldgjá, the hydromagmatic pyroclasts have an additional specific surface energy of 3–14 kJ kg^{-1} compared to the dry, magmatic deposits. Using these observations, we calculated the energy expended in hydrofragmentation resulting from interaction between pyroclasts and entrained meltwater by simulating a volcanic jet passing through a column of meltwater. By matching the calculated hydrofragmentation energy with the additional surface energy and by matching the simulated plume height with the interpreted values, 17–18 km, from pyroclast dispersal we estimate the entrained water-to-melt mass ratio of 1–2. We find that the water-to-melt mass ratio has a significant impact on volcanic plume buoyancy and determines whether a plume collapses or ascends above the tropopause. Our simulations show that for water-to-melt mass ratios below two, water entrainment slightly increases the plume height in comparison to dry plumes, whereas, water-to-melt mass ratios above two cause the plume to collapse.

Data Availability Statement

Data used in this work are available through Moreland et al., 2019.

Acknowledgments
T. J. Jones was supported by a Rice University Fellowship and a Royal Society research grant (RGS\R1\211015). WMM was supported by Icelandic Research Fund (Rannsóknasjóður), Grant No. 1100770061, and the South Iceland Research Fund (Háskólafélag Suðurlands).

References

Aravena, A., Vitturi, M. D., Cioni, R., & Neri, A. (2018). Physical constraints for effective magma-water interaction along volcanic conduits during silicic explosive eruptions. *Geology*, *46*(10), 867–870. https://doi.org/10.1130/G45065.1

Board, S., Farmer, C., & Poole, D. (1974). Fragmentation in thermal explosions. *International Journal of Heat and Mass Transfer*, *17*(2), 331–339. https://doi.org/10.1016/0017-9310(74)90094-5

Bruce, P. M., & Huppert, H. E. (1989). Thermal control of basaltic fissure eruptions. *Nature*, *342*, 665–667. https://doi.org/10.1038/342665a0

Budd, D. A., Troll, V. R., Dahren, B., & Burchardt, S. (2016). Persistent multitiered magma plumbing beneath Katla volcano, Iceland. *Geochemistry, Geophysics, Geosystems*, *17*(3), 966–980. https://doi.org/10.1002/2015GC006118

Buhl, E., Sommer, F., Poelchau, M. H., Dresen, G., & Kenkmann, T. (2014). Ejecta from experimental impact craters: Particle size distribution and fragmentation energy. *Icarus*, *237*, 131–142. https://doi.org/10.1016/j.icarus.2014.04.039

Büttner, R., Dellino, P., La Volpe, L., Lorenz, V., & Zimanowski, B. (2002). Thermohydraulic explosions in phreatomagmatic eruptions as evidenced by the comparison between pyroclasts and products from Molten Fuel Coolant Interaction experiments. *Journal of Geophysical Research*, *107*(B11), ECV 5-1–ECV 5-14. https://doi.org/10.1029/2001JB000511

Büttner, R., Dellino, P., Raue, H., Sonder, I., & Zimanowski, B. (2006). Stress-induced brittle fragmentation of magmatic melts: Theory and experiments. *Journal of Geophysical Research*, *111*(B8), B08204. https://doi.org/10.1029/2005JB003958

Büttner, R., & Zimanowski, B. (1998). Physics of thermohydraulic explosions. *Physical Review E*, *57*(5), 5726–5729. https://doi.org/10.1103/PhysRevE.57.5726

Cahalan, R. C., & Dufek, R. (2021). Explosive submarine eruptions: The role of condensable gas jets in underwater eruptions. *Journal of Geophysical Research: Solid Earth*, *126*(2), e2020JB020969. https://doi.org/10.1029/2020JB020969

Carey, R. J., Houghton, B. F., & Thordarson, T. (2009). Abrupt shifts between wet and dry phases of the 1875 eruption of Askja Volcano: Microscopic evidence for macroscopic dynamics. *Journal of Volcanology and Geothermal Research*, *184*(3–4), 256–270. https://doi.org/10.1016/j.jvolgeores.2009.04.003

Chester, J. S., Chester, F. M., & Kronenberg, A. K. (2005). Fracture surface energy of the Punchbowl fault, San Andreas system. *Nature*, *437*(7055), 133–136. https://doi.org/10.1038/nature03942

Colombier, M., Scheu, B., Kueppers, U., Cronin, S. J., Mueller, S. B., Hess, K., et al. (2019). In situ granulation by thermal stress during subaqueous volcanic eruptions. *Geology*, *47*(2), 179–182. https://doi.org/10.1130/G45503.1

Colombier, M., Scheu, B., Wadsworth, F. B., Cronin, S., Vasseur, J., Dobson, K. J., et al. (2018). Vesiculation and quenching during Surtseyan eruptions at Hunga Tonga-Hunga Ha'apai volcano, Tonga. *Journal of Geophysical Research: Solid Earth*, *123*(5), 3762–3779. https://doi.org/10.1029/2017JB015357

Dürig, T., Sonder, I., Zimanowski, B., Beyrichen, H., & Büttner, R. (2012). Generation of volcanic ash by basaltic volcanism. *Journal of Geophysical Research: Solid Earth*, *117*(B1), B01204. https://doi.org/10.1029/2011JB008628

Eckhoff, R. K. (2016). Water vapour explosions – a brief review. *Journal of Loss Prevention in the Process Industries*, *40*, 188–198. https://doi.org/10.1016/j.jlp.2015.11.017

Edwards, B. R., Gudmundsson, M. T., & Russell, J. K. (2015). Glaciovolcanism. In *The encyclopedia of volcanoes* (pp. 377–393). Elsevier. https://doi.org/10.1016/B978-0-12-385938-9.00020-1

Edwards, B. R., Russell, J. K., & Simpson, K. (2011). Volcanology and petrology of Mathews Tuya, northern British Columbia, Canada: Glaciovolcanic constraints on interpretations of the 0.730 ma Cordilleran paleoclimate. *Bulletin of Volcanology*, *73*, 479–496. https://doi.org/10.1007/s00445-010-0418-z

Eibl, E. P., Bean, C. J., Jónsdóttir, I., Höskuldsson, A., Thordarson, T., Coppola, D., et al. (2017). Multiple coincident eruptive seismic tremor sources during the 2014–2015 eruption at Holuhraun, Iceland. *Journal of Geophysical Research: Solid Earth*, *122*, 2972–2987. https://doi.org/10.1002/2016JB013892

Feistel, R., & Wagner, W. (2006). A new equation of state for H_2O ice ih. *Journal of Physical and Chemical Reference Data*, *35*(2), 1021–1047. https://doi.org/10.1063/1.2183324

Fitch, E. P., & Fagents, S. A. (2020). Characteristics of rootless cone tephra emplaced by high-energy lava–water explosions. *Bulletin of Volcanology*, *82*(8). https://doi.org/10.1007/s00445-020-01393-5

Fitch, E. P., Fagents, S. A., Thordarson, T., & Hamilton, C. W. (2017). Fragmentation mechanisms associated with explosive lava–water interactions in a lacustrine environment. *Bulletin of Volcanology*, *79*(1). https://doi.org/10.1007/s00445-016-1087-3

Grady, D. E. (1982). Local inertial effects in dynamic fragmentation. *Journal of Applied Physics*, *53*(1), 322–325. https://doi.org/10.1063/1.329934

Graettinger, A. H., Skilling, I., McGarvie, D., & Höskuldsson, Á. (2013). Subaqueous basaltic magmatic explosions trigger phreatomagmatism: A case study from Askja, Iceland. *Journal of Volcanology and Geothermal Research*, *264*, 17–35. https://doi.org/10.1016/j.jvolgeores.2013.08.001

Griffith, A. A. (1921). VI. The phenomena of rupture and flow in solids. *Philosophical Transactions of the Royal Society of London - Series A: Containing Papers of a Mathematical or Physical Character*, *221*(582–593), 163–198. https://doi.org/10.1098/rsta.1921.0006

Gudmundsson, M. T. (2003). Melting of ice by magma-ice-water interactions during subglacial eruptions as an indicator of heat transfer in subaqueous eruptions. *Geophysical Monograph-American Geophysical Union*, *140*, 61–72. https://doi.org/10.1029/140gm04

Gudmundsson, M. T., Sigmundsson, F., & Björnsson, H. (1997). Ice–volcano interaction of the 1996 Gjálp subglacial eruption, Vatnajökull, Iceland. *Nature*, *389*(6654), 954–957. https://doi.org/10.1038/40122

Gudmundsson, M. T., Sigmundsson, F., Björnsson, H., & Högnadóttir, T. (2004). The 1996 eruption at Gjálp, Vatnajökull ice cap, Iceland: Efficiency of heat transfer, ice deformation and subglacial water pressure. *Bulletin of Volcanology*, *66*(1), 46–65. https://doi.org/10.1007/s00445-003-0295-9

Gudmundsson, M. T., Thordarson, T., Höskuldsson, Á., Larsen, G., Björnsson, H., Prata, F. J., et al. (2012). Ash generation and distribution from the April-May 2010 eruption of Eyjafjallajökull, Iceland. *Scientific Reports*, *2*(1), 572. https://doi.org/10.1038/srep00572

Hammer, C. U. (1984). Traces of Icelandic eruptions in the Greeland ice sheet. *Jökull Journal*, 51–65.

Hartley, M. E., Maclennan, J., Edmonds, M., & Thordarson, T. (2014). Reconstructing the deep CO_2 degassing behaviour of large basaltic fissure eruptions. *Earth and Planetary Science Letters*, *393*, 120–131. https://doi.org/10.1016/j.epsl.2014.02.031

Head, J. W., & Wilson, L. (2003). Deep submarine pyroclastic eruptions: Theory and predicted landforms and deposits. *Journal of Volcanology and Geothermal Research*, *121*(3–4), 155–193. https://doi.org/10.1016/S0377-0273(02)00425-0

Houghton, B., & Carey, R. (2019). Physical constraints for effective magma-water interaction along volcanic conduits during silicic explosive eruptions: Comment. *Geology*, *47*(5). https://doi.org/10.1130/G46033C.1

Houghton, B., & Hackett, W. (1984). Strombolian and phreatomagmatic deposits of Ohakune craters, Ruapehu, New Zealand: A complex interaction between external water and rising basaltic magma. *Journal of Volcanology and Geothermal Research*, *21*, 207–231. https://doi.org/10.1016/0377-0273(84)90023-4

Houghton, B., White, J. D., & Eaton, A. R. V. (2015). Phreatomagmatic and related eruption styles. In *The encyclopedia of volcanoes* (pp. 377–552). Elsevier. https://doi.org/10.1016/b978-0-12-385938-9.00030-4

Iskhakov, A., Melikhov, V., & Melikhov, O. (2019). Hugoniot analysis of energetic molten lead-water interaction. *Annals of Nuclear Energy*, *129*, 437–449. https://doi.org/10.1016/j.anucene.2019.02.018

Jones, T., & Llewellin, E. (2021). Convective tipping point initiates localization of basaltic fissure eruptions. *Earth and Planetary Science Letters*, *553*, 116637. https://doi.org/10.1016/j.epsl.2020.116637

Jones, T. J., Llewellin, E. W., Houghton, B. F., Brown, R. J., & Vye-Brown, C. (2017). Proximal lava drainage controls on basaltic fissure eruption dynamics. *Bulletin of Volcanology*, *79*. https://doi.org/10.1007/s00445-017-1164-2

Kokelaar, P. (1986). Magma-water interactions in subaqueous and emergent basaltic. *Bulletin of Volcanology*, *48*(5), 275–289. https://doi.org/10.1007/BF01081756

Koshizuka, S., Ikeda, H., & Oka, Y. (1999). Numerical analysis of fragmentation mechanisms in vapor explosions. *Nuclear Engineering and Design*, *189*, 423–433. https://doi.org/10.1016/s0029-5493(98)00270-2

Koyaguchi, T., & Woods, A. W. (1996). On the formation of eruption columns following explosive mixing of magma and surface-water. *Journal of Geophysical Research*, *101*(3), 5561–5574. https://doi.org/10.1029/95jb01687

Larsen, G. (2000). Holocene eruptions within the Katla volcanic system, south Iceland: Characteristics and environmental impact. *Jökull*, *49*, 1–28.

Liu, E., Cashman, K., Rust, A., & Gislason, S. (2015). The role of bubbles in generating fine ash during hydromagmatic eruptions. *Geology*, *43*(3), 239–242. https://doi.org/10.1130/G36336.1

Liu, E., Cashman, K. V., Rust, A. C., & Höskuldsson, A. (2017). Contrasting mechanisms of magma fragmentation during coeval magmatic and hydromagmatic activity: The hverfjall fires fissure eruption, Iceland. *Bulletin of Volcanology*, *79*(10), 68. https://doi.org/10.1007/s00445-017-1150-8

Mastin, L., Christiansen, R. L., Thornber, C., Lowenstern, J., & Beeson, M. (2004). What makes hydromagmatic eruptions violent? Some insights from the Keanakako'i ash, Kilauea volcano, Hawai'i. *Journal of Volcanology and Geothermal Research*, *137*(1–3), 15–31. https://doi.org/10.1016/j.jvolgeores.2004.05.015

Mastin, L., Guffanti, M., Servranckx, R., Webley, P., Barsotti, S., Dean, K., et al. (2009). A multidisciplinary effort to assign realistic source parameters to models of volcanic ash-cloud transport and dispersion during eruptions. *Journal of Volcanology and Geothermal Research*, *186*(1–2), 10–21. https://doi.org/10.1016/j.jvolgeores.2009.01.008

Mastin, L., Spieler, O., & Downey, W. (2009). An experimental study of hydromagmatic fragmentation through energetic, non-explosive magma–water mixing. *Journal of Volcanology and Geothermal Research*, *180*(2–4), 161–170. https://doi.org/10.1016/j.jvolgeores.2008.09.012

Mastin, L. G. (2007). A user-friendly one-dimensional model for wet volcanic plumes. *Geochemistry, Geophysics, Geosystems*, *8*(3). https://doi.org/10.1029/2006GC001455

McCarthy, D., & Breen, A. (1997). An evaluation of astronomical observations in the Irish annals. *Vistas in Astronomy*, *41*(1), 117–138. https://doi.org/10.1016/S0083-6656(96)00052-9

Meignen, R., Raverdy, B., Picchi, S., & Lamome, J. (2014). The challenge of modeling fuel–coolant interaction: Part II – steam explosion. *Nuclear Engineering and Design*, *280*, 528–541. https://doi.org/10.1016/j.nucengdes.2014.08.028

Miller, J. (1989). *The 10th century eruption of Eldgjá, southern Iceland*. Nordic Volcanological Institute, University of Iceland.

Moreland, W. (2017). *Explosive activity in flood lava eruptions: A case study of the 10th century Eldgjá eruption, Iceland (PhD thesis,)*. University of Iceland.

Moreland, W., Thordarson, T., Houghton, B., & Larsen, G. (2019). Driving mechanisms of subaerial and subglacial explosive episodes during the 10th century Eldgjá fissure eruption, southern Iceland. *Volcanica*, *2*(2), 129–150. https://doi.org/10.30909/vol.02.02.129150

Morton, B. R. (1959). Forced plumes. *Journal of Fluid Mechanics*, *5*, 151–163. https://doi.org/10.1017/s002211205900012x

Neal, C. A., Brantley, S. R., Antolik, L., Babb, J. L., Burgess, M., Calles, K., & Damby, D. (2019). Volcanology: The 2018 rift eruption and summit collapse of Kilauea volcano. *Science*, *363*. https://doi.org/10.1126/science.aav7046

Oman, L., Robock, A., Stenchikov, G. L., & Thordarson, T. (2006). High-latitude eruptions cast shadow over the African monsoon and the flow of the Nile. *Geophysical Research Letters*, *33*(18). https://doi.org/10.1029/2006GL027665

Oppenheimer, C., Orchard, A., Stoffel, M., Newfield, T. P., Guillet, S., Corona, C., & Büntgen, U. (2018). The Eldgjá eruption: Timing, long-range impacts and influence on the Christianisation of Iceland. *Climatic Change*, *147*(3–4), 369–381. https://doi.org/10.1007/s10584-018-2171-9

Parcheta, C., Fagents, S., Swanson, D. A., Houghton, B. F., & Ericksen, T. (2015). *Hawaiian fissure fountains: Quantifying vent and shallow conduit geometry, episode 1 of the 1969-1974 Mauna ulu eruption*. https://doi.org/10.1002/9781118872079.ch17

Pedrazzi, D., Martí, J., & Geyer, A. (2013). Stratigraphy, sedimentology and eruptive mechanisms in the tuff cone of El Golfo (Lanzarote, Canary Islands). *Bulletin of Volcanology*, *75*(7), 740. https://doi.org/10.1007/s00445-013-0740-3

Pyle, D. M. (1995). Assessment of the minimum volume of tephra fall deposits. *Journal of Volcanology and Geothermal Research*, *69*(3–4), 379–382. https://doi.org/10.1016/0377-0273(95)00038-0

Rowell, C. R., Jellinek, A. M., Hajimirza, S., & Aubry, T. J. (2021). External surface water influence on explosive eruption dynamics, with implications for stratospheric Sulfur delivery and volcano-climate feedback. *EarthArXiv*. https://doi.org/10.31223/X5XP6Z

Russell, J. K., Edwards, B. R., & Porritt, L. A. (2013). Pyroclastic passage zones in glaciovolcanic sequences. *Nature Communications*, *4*(1), 1788. https://doi.org/10.1038/ncomms2829

Rust, A. C., & Cashman, K. V. (2011). Permeability controls on expansion and size distributions of pyroclasts. *Journal of Geophysical Research*, *116*(11), 1–17. https://doi.org/10.1029/2011JB008494

Schmid, A., Sonder, I., Seegelken, R., Zimanowski, B., Büttner, R., Gudmundsson, M. T., & Oddsson, B. (2010). Experiments on the heat discharge at the dynamic magma-water-interface. *Geophysical Research Letters*, *37*(20). https://doi.org/10.1029/2010GL044963

Sheridan, M. F., & Wohletz, K. H. (1981). Hydrovolcanic explosions: The systematics of water-pyroclast Equilibration. *Science*, *212*(4501), 1387–1389. https://doi.org/10.1126/science.212.4501.1387

Sheridan, M. F., & Wohletz, K. H. (1983). Hydrovolcanism: Basic considerations and review. *Journal of Volcanology and Geothermal Research*, *17*(1–4), 1–29. https://doi.org/10.1016/0377-0273(83)90060-4

Sigurdardóttir, S. S., & Gudmundsson, M. T. (2015). Mapping of the Eldgjá lava flow on Myrdalssandur with magnetic surveying. *Jökull*, *65*, 61–71.

Smellie, J., Johnson, J., McIntosh, W., Esser, R., Gudmundsson, M., Hambrey, M., & van Wyk de Vries, B. (2008). Six million years of glacial history recorded in volcanic lithofacies of the James Ross Island volcanic Group, Antarctic Peninsula. *Palaeogeography, Palaeoclimatology, Palaeoecology*, *260*(1–2), 122–148. https://doi.org/10.1016/j.palaeo.2007.08.011

Sonder, I., Harp, A. G., Graettinger, A. H., Moitra, P., Valentine, G. A., Büttner, R., & Zimanowski, B. (2018). Meter-scale experiments on magma-water interaction. *Journal of Geophysical Research: Solid Earth*, *123*(12), 10597–10615. https://doi.org/10.1029/2018JB015682

Stothers, R. B. (1998). Far reach of the tenth century Eldgjá eruption. *Iceland. Climate Change*, *39*, 715–726. https://doi.org/10.1023/A:1005323724072

Thordarson, T., & Hoskuldsson, A. (2008). Postglacial volcanism in Iceland. *Jökull*, *58*, 228.

Thordarson, T., & Larsen, G. (2007). Volcanism in Iceland in historical time: Volcano types, eruption styles and eruptive history. *Journal of Geodynamics*, *43*(1), 118–152. https://doi.org/10.1016/j.jog.2006.09.005

Thordarson, T., Miller, D., Larsen, G., Self, S., & Sigurdsson, H. (2001). New estimates of Sulfur degassing and atmospheric mass-loading by the 934 AD Eldgjá eruption, Iceland. *Journal of Volcanology and Geothermal Research*, *108*(1–4), 33–54. https://doi.org/10.1016/S0377-0273(00)00277-8

Toramaru, A. (1990). Measurement of bubble size distributions in vesiculated rocks with implications for quantitative estimation of eruption processes. *Journal of Volcanology and Geothermal Research*, *43*(1–4), 71–90. https://doi.org/10.1016/0377-0273(90)90045-h

Van Eaton, A. R., Herzog, M., Wilson, C. J., & McGregor, J. (2012). Ascent dynamics of large phreatomagmatic eruption clouds: The role of microphysics. *Journal of Geophysical Research: Solid Earth*, *117*(3), 1–23. https://doi.org/10.1029/2011JB008892

van Otterloo, J., Cas, R. A., & Scutter, C. R. (2015). The fracture behaviour of volcanic glass and relevance to quench fragmentation during formation of hyaloclastite and phreatomagmatism. *Earth-Science Reviews*, *151*, 79–116. https://doi.org/10.1016/j.earscirev.2015.10.003

Wagner, W., & Pruß, A. (2002). The IAPWS formulation 1995 for the thermodynamic properties of Ordinary water substance for general and scientific use. *Journal of Physical and Chemical Reference Data*, *31*(2), 387–535. https://doi.org/10.1063/1.1461829

Wilson, A. M., & Russell, J. K. (2018). Quaternary glaciovolcanism in the Canadian Cascade volcanic arc–Paleoenvironmental implications. *Field Volcanology: A tribute to the distinguished career of Don Swanson: Geological Society of America Special Papers*, *538*, 133–157.

Wilson, L., Sparks, R. S. J., & Walker, G. P. L. (1980). Explosive volcanic eruptions – IV. The control of magma properties and conduit geometry on eruption column behaviour. *Geophysical Journal International*, *63*(1), 117–148. https://doi.org/10.1111/j.1365-246X.1980.tb02613.x

Wohletz, K. (1986). Explosive magma-water interactions: Thermodynamics, explosion mechanisms, and field studies. *Bulletin of Volcanology*, *48*(5), 245–264. https://doi.org/10.1007/BF01081754

Wohletz, K. (2002). Water/magma interaction: Some theory and experiments on peperite formation. *Journal of Volcanology and Geothermal Research*, *114*(1–2), 19–35. https://doi.org/10.1016/S0377-0273(01)00280-3

Wohletz, K., & McQueen, R. (1984). Volcanic and stratospheric dustlike particles produced by experimental water-melt interactions:VASDPP 2.0. *Geology*, *12*(10), 5912. https://doi.org/10.1130/0091-7613(1984)12<591:vasdpp>2.0.CO;2

Wohletz, K., & Sheridan, M. F. (1983). Hydrovolcanic explosions; II, Evolution of basaltic tuff rings and tuff cones. *American Journal of Science*, *283*(5), 385–413. https://doi.org/10.2475/ajs.283.5.385

Wohletz, K., Zimanowski, B., & Büttner, R. (2013). Magma-water interactions. In *Modeling volcanic process* (pp. 230–257). Cambridge University Press.

Woods, A. (1988). The fluid dynamics and thermodynamics of eruption columns. *Bulletin of Volcanology*, *50*(3), 169–193. https://doi.org/10.1007/BF01079681

Yew, C. H., & Taylor, P. A. (1994). A thermodynamic theory of dynamic fragmentation. *International Journal of Impact Engineering*, *15*(4), 385–394. https://doi.org/10.1016/0734-743X(94)80023-3

Zielinski, G. A., Germani, M. S., Larsen, G., Baillie, M. G., Whitlow, S., Twickler, M. S., & Taylor, K. (1995). Evidence of the Eldgjá (Iceland) eruption in the GISP2 Greenland ice core: Relationship to eruption processes and climatic conditions in the tenth century. *The Holocene*, *5*(2), 129–140. https://doi.org/10.1177/095968369500500201

Zimanowski, B., Büttner, R., & Lorenz, V. (1997). Premixing of magma and water in MFCI experiments. *Bulletin of Volcanology*, *58*(6), 491–495. https://doi.org/10.1007/s004450050157